Controller Verification of a Smart-Grid Compatible 200 kHz Single-stage Photovoltaic Microinverter

Daniel Zakzewski, Rakesh Resalayyan, Arafat Hasnain, Chanaka Singhabahu, Alireza Khaligh
Maryland Power Electronics Laboratory, Department of Electrical and Computer Engineering, The Institute for Systems Research
University of Maryland
College Park, United States
Email: {dzak,rakeshr,hasnain,chanaka,khaligh}@umd.edu, URL: khaligh.umd.edu

***Abstract*—This paper presents control system design, implementation, and experimental validation of a single-stage 400 W, 200 kHz solar photovoltaic (PV) microinverter using hardware-in-the-loop (HIL) and hardware testing. The selected circuit topology is based on a Gallium Nitride (GaN) direct-matrix based dual active bridge (DAB) converter with a low voltage active power decoupler (APD) circuit. Control performance is verified, smart-grid compatibility is tested, and circuit operation is confirmed. Controller HIL (CHIL) is shown to aid in a complex power electronics system design by 1) enabling detailed control development prior to hardware implementation, 2) expanding the use of automated testing, and 3) increasing confidence in control performance prior to prototype testing. Altogether, these factors make HIL a valuable tool in complex power electronic designs.**

***Index Terms*—PV, solar, microinverter, HIL, CHIL, smart-grid, control of power electronic converters, photovoltaic inverters and microinverters, DAB, direct-matrix**

I. Introduction

Globally, residential roof-top PV growth was 30% in 2021, significantly outperforming that of industrial and commercial PV growth [1]. For residential applications, microinverters tend to be preferred over centralized inverters and string inverters for their maximum power point tracking (MPPT) performance, single inverter fault tolerance, elimination of low-frequency transformers, and simplicity of installation [2]–[4].

As this penetration of PV microinverters and other distributed energy resources (DER) continues, there is an increased need for advanced smart-grid control features to minimize the potential negative impacts DERs on the grid. California Rule 21 and IEEE 1547-2018 require DERs to include features such as voltage ride-through, frequency ride-through, grid support functions, anti-islanding protection, and rate limits [5]–[7].

In this paper, controller hardware-in-the-loop (CHIL) is used to design, implement, and test a control system for a grid-tied PV microinverter by enabling evaluation of the control implementation in a simulated hardware environment. Additionally, the real-time, or near real-time, simulation speed of modern HIL equipment increases the scope and scale of tests and allows for testing of the smart-grid features, modulation approaches, and MPPT algorithms in a rapid and automated manner. In contrast, modeling and simulation is suitable for control algorithms design, but typically both the controller and plant assume idealized conditions. Furthermore, the time required in more complex simulations will limit the scope of tests performed. Conversely, hardware testing includes many non-idealities which make detailed control system evaluation more difficult and introduces risks of destruction. Hardware testing is then used to further confirm controller performance following CHIL testing. Therefore, HIL is a useful intermediate between full-simulation and hardware testing. [8]–[11].

This material is based upon work supported by the U.S. Department of Energy's Office of Energy Efficiency and Renewable Energy (EERE) under the Solar Energy Technologies Office Award Number DE-EE0008350.

II. Control of Proposed Microinverter Design

The next generation of residential microinverters should reduce the cost, increase power density, increase reliability, and comply with U.S. grid-side standards such as California Rule 21. Additionally, the high-level objectives for the microinverter design are 400 W output, maximum power point voltages between 30 V and 60 V, and a nominal grid interface voltage of 240 Vac.

Fig. 1 shows a proposed design for the next generation microinverter. In the proposed design, a direct-matrix DAB [12] converts the PV's low voltage dc to 240 V, 60 Hz through a high frequency transformer. Use of Gallium Nitrite (GaN) semiconductors and advanced control, which ensures zero-voltage-switching (ZVS) over the entire operating range, enables a switching frequency of 200 kHz, thereby reducing the required size of magnetics. The direct-matrix DAB converter consists of switches S_1–S_8, the high frequency transformer with leakage inductance L_{lk}, and half-bridge capacitors C_{hb}. An active power decoupler (APD) circuit is used to remove

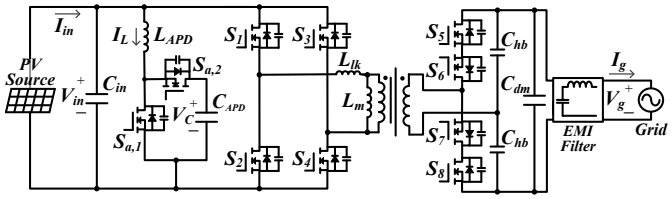

Fig. 1. Circuit diagram for proposed next generation PV microinverter.

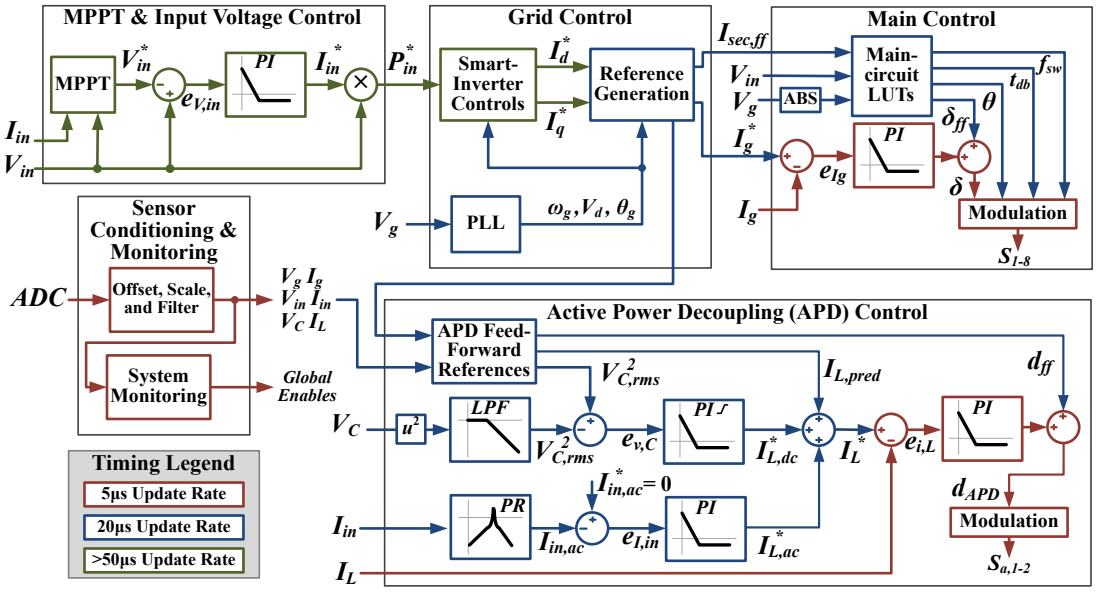

Fig. 2. Control diagram for proposed PV microinverter design, consisting of a direct-matrix DAB and APD circuit. Colors on the diagram indicate the update rate used by the controller.

double line frequency power pulsation at the PV terminals [13]. The APD circuit consists of switches $S_{a,1}$ and $S_{a,2}$, inductor L_{APD}, and capacitor C_{APD}.

The proposed microinverter design is intended to be smart-grid compatible. CA Rule 21 [6] specifies design and operation requirements for generating facilities that are to be connected to a distribution system. The most applicable requirements for microinverters are found in Section Hh. The key features for a smart-grid compatible microinverter are:

- Stability Check (Section Hh.1.a.ii)
- Voltage Ride Through (Section Hh.2.b)
- Frequency Ride Through (Section Hh.2.f)
- Volt/var (Section Hh.2.j)
- Frequency Watt (Section Hh.2.l)
- Volt Watt (Section Hh.2.m)
- Unintended Island Prevention (Section Hh.1.a.iii)
- Ramp Rates & Soft Start (Section Hh.2.k)
- Specified Power Factor (Section Hh.2.i)

The implementation of these functions is simplified when using a synchronous reference frame, because the specifications are either in terms of synchronous values (e.g., active or reactive power) or readily translate to synchronous frames (e.g., power factor, ramp rates). Therefore, the control is designed to operate in synchronous frame, using direct current I_d and quadrature axis current I_q commands. The synchronous current reference values are based on the MPPT algorithm, grid conditions, and smart-grid compliance.

Fig. 2 shows the final control diagram for the microinverter design. There are six sensors used in the control system: input voltage V_{in}, input current I_{in}, grid voltage V_g, output grid current I_g, APD capacitor voltage V_C, and APD inductor current I_L. The Sensor Conditioning & Monitoring subsystem (Fig. 2) provides input scaling and noise filtering for analog-to-digital sensor (ADC) values and tracks the values of the sensors to ensure they are within tolerable ranges. The MPPT and Input Voltage Control subsystem uses an MPPT algorithm, in this case perturb and observe (P&O) [14], to identify and track the maximum power point of the PV by modifying the power reference P^*_{in}. The Grid Control subsystem tracks grid behavior and implements the features required for smart-grid compatibility. The Reference Generator subsystem calculates feed-forward and reference values. The Main Control subsystem performs dual-phase shift modulation for the DAB using a look-up-table (LUT) and a closed loop controller.

To modulate the direct-matrix DAB converter, the stationary reference frame is required. The desired output current I_g (2) is used for closed loop control. For feed-forward control, the DAB output current I_{sec} (5) includes the desired output current and a compensating quadrature axis current $I_{q_{comp}}$ (3). This current compensates for the reactive power supplied by the capacitive circuit elements located between the DAB and the grid connection. The following summarizes the DAB stationary reference frame signals:

$$V_g = V_d \sin(\theta_g) \tag{1}$$

$$I_g = I_d \sin(\theta_g) + I_q \cos(\theta_g) \tag{2}$$

$$I_{q_{comp}} = V_d \omega_g \left(\frac{C_{hb}}{2} + C_{dm} \right) \tag{3}$$

$$I_{q_{all}} = I_q + I_{q_{comp}} \tag{4}$$

$$I_{sec} = I_d \sin(\theta_g) + I_{q_{all}} \cos(\theta_g) \tag{5}$$

Control of the APD circuit uses feed-forward control. The APD duty ratio d_{ff} and inductor current I_L are calculated based on the power that the APD should decouple P_{APD}. The APD decoupling power is equal to the ac portion of the

power transferred by the direct-matrix DAB. The dc portion of the DAB power $P_{DAB_{dc}}$ is provided by the PV. The current of the APD inductor is then calculated based on the input voltage and APD decoupling power.

$$P_{APD} = P_{DAB_{dc}} - -P_{DAB} \tag{6}$$
$$= \frac{V_g I_{sec} - I_d V_d}{2} \tag{7}$$
$$= \frac{V_d}{2}\left[(I_d \cos(2\theta_g) - I_{q_{all}} \sin(2\theta_g)\right] \tag{8}$$
$$I_L = \frac{P_{APD}}{V_{in}} \tag{9}$$

The APD capacitor voltage is derived from the APD energy, which is a summation of the decoupling energy $E_{C_{ac}}$ and the dc energy of the capacitor $E_{C_{dc}}$. The dc energy term is based on the desired APD capacitor rms voltage $V_{C_{rms}}$. The APD operates as a boost converter, so $V_{C_{rms}}$ must be set to ensure V_C is always greater than V_{in}.

$$E_{C_{ac}} = \int P_{APD}\, dt \tag{10}$$
$$= \frac{1}{\omega_g}\int P_{APD}\, d\theta_g \tag{11}$$
$$= \frac{V_d}{4\omega_g}\left[I_d \sin(2\theta_g) + I_{q_{all}} \cos(2\theta_g)\right] \tag{12}$$
$$E_{C_{dc}} = \frac{1}{2} C_{APD} V_{C_{rms}}^2 \tag{13}$$

$$V_C = \sqrt{\frac{2(E_{C_{ac}} + E_{C_{dc}})}{C_{APD}}} \tag{14}$$
$$= \sqrt{V_d \frac{I_d \sin(2\theta_g) + I_{q_{all}} \cos(2\theta_g)}{2 C_{APD} \omega_g} + V_{C_{rms}}^2} \tag{15}$$

Finally, the APD duty ratio is calculated using the well-known boost-converter equation which relates a boost-converter's duty cycle to its input and output voltages.

$$d_{ff} = 1 - \frac{V_{in}}{V_C} \tag{16}$$

III. Control Hardware Testing

The microinverter control system uses five proportional integral controllers, several filters of varying design, and many predictive controls. Complexity of control, non-linear behaviors within the plant, and a set of demanding performance goals, make stable control parameter selection a challenge. Therefore, early testing of control implementation is vital for a successful next generation microinverter design.

A. Controller Hardware in the Loop

This design uses CHIL to enable detailed control system evaluation early in the design process. In CHIL, a digital signal processor (DSP), or other control hardware, interfaces with a real time simulator (RTS) which simulates the microinverter circuit and its interfaces. Fig. 3 shows the test configuration for the CHIL testing. The RTS used is a Opal-RT OP4510. The

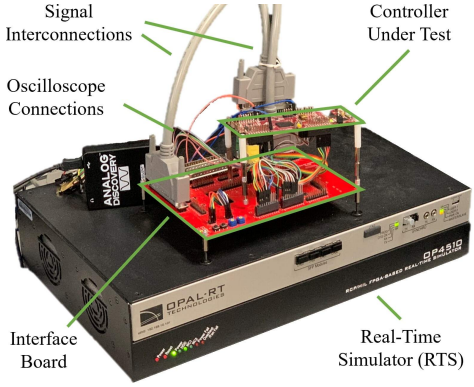

Fig. 3. Hardware configuration for controller hardware-in-the-loop testing. The real time simulator is a Opal RT OP4510, the controller under test is a Texas Instruments LAUNCHXL-F28379D, and the oscilloscopes used are a Digilent's Analog Discovery and an Agilent DSO-X 2014A.

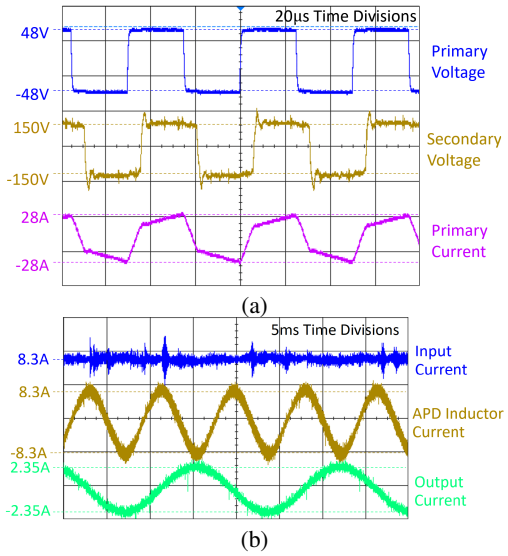

Fig. 4. Controller hardware-in-the-loop waveforms of the direct-matrix DAB operation showing (a) switching-frequency waveforms of the high-frequency transformer near peak power, and (b) the fundamental (60 Hz) currents of the microinverter including input current sourced by a PV.

RTS simulates the system plant including the microinverter circuit, PV, and grid. The OP4510 uses an FPGA-based circuit simulator capable of real-time simulation step sizes of 200 ns. The microinverter circuit model, including PV source, grid interfaces, and input/outputs, achieve a simulation step size of 300 ns. Additionally, the OP4510 uses a CPU for additional calculations with step sizes of above 10 µs [15]. Grid commands, PV emulation, test configuration, and result checking occurs in the CPU. The controller under test here is a Texas Instruments LAUNCHXL-F28379D. The only data exchanged between the controller under test and the RTS are controller gate signals and emulated sensor results. An interface board is used to level shift these signals. Signals are observed on an oscilloscope and may also be observed from RTS's user interfaces.

Although a step size of 300 ns may be sufficient to capture

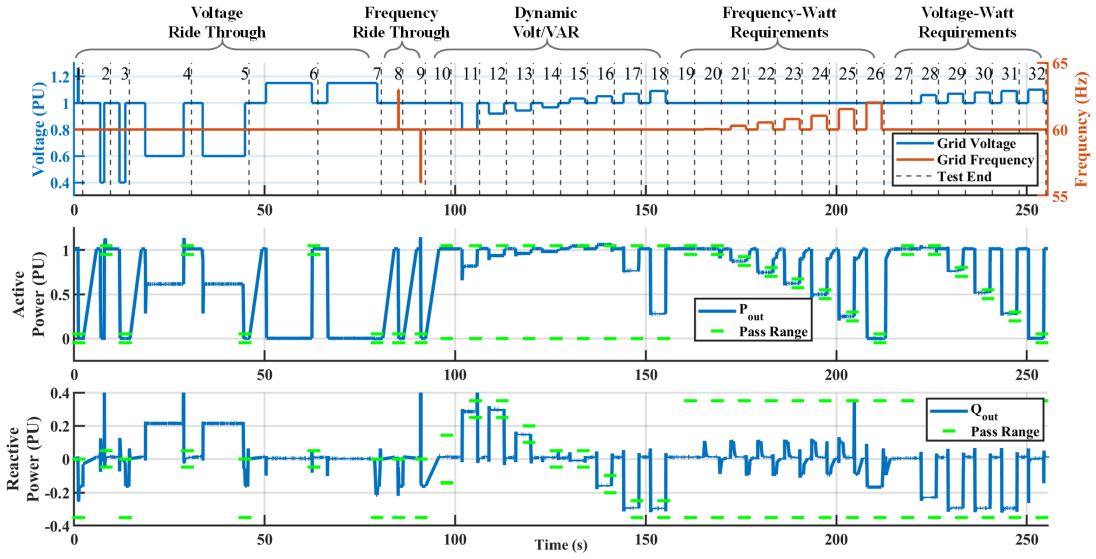

Fig. 5. Results of automated smart-grid testing, with plots indicating test conditions (upper) and exported active (middle) and reactive (lower) power.

the behavior of the 200 kHz DAB, additional fidelity is desired. Therefore, a 10:1 time factor is used to effectively achieve a 30 ns step size of the circuit model, thereby increasing the samples per switching cycle from 16.67 to 166.67. The control is scaled by slowing the controller update rate to a tenth its designed speed. The plant is scaled by shifting all inductance and capacitance circuit parameters up an order of magnitude, which increases all the circuit time constants by a factor of 10. This increase in resolution ensures that dual phase shift modulation commands are sufficiently represented to give confidence of controller performance. This is considered a suitable resolution increase because the resolution of the digital controller's gate signals, 10 ns, is only 1/3 of the RTS's effective simulation step-size.

The microinverter control design was tested starting with simplified open-loop control of individual circuits (i.e., APD or DAB separately) and simplified interfaces (i.e., DC source and resistive load), and incrementally progressing further until the complete design shown in Fig. 2. This incremental control design, implementation, and test approach was enabled by CHIL in that the realistic in controller limitations were always present, while the plant gradually increased in complexity. Therefore, individual loops could be tested and integrated until a complete control system was formed.

Fig. 4 shows simulated microinverter waveforms using CHIL and the 10:1 time factor approach. Fig. 4 (a) shows the measured DAB waveforms, specifically for a grid voltage of 300V, when the no primary phase shift is required. Fig. 4 (b) shows the resulting microinverter performance at rated power and nominal grid voltage. The input current waveform confirms that the APD is properly decoupling AC power from the input. These CHIL results verify the inner control loops and modulation controls of the microinverter control hardware are operating as designed.

After fundamental operation of the microinverter was verified, smart-grid functionality was tested. Fig. 5 shows the results of a series of automated smart-grid tests performed with CHIL. These tests evaluate a reduced set of grid conditions, and thus do not fully validate all smart-grid features. The upper plot shows the commanded grid frequency and grid voltage for each test. The middle and lower plots show the active and reactive power output of the microinverter, measured at the grid. The green lines indicate the test acceptance ranges for each. In all cases, the microinverter passed the tests. Specific tests, as required by California Rule 21 [6], performed were:

- Voltage ride through (tests 1-7)
- Frequency ride through (tests 8-9)
- Volt/var (tests 10-17)
- Frequency watt (tests 18-25)
- Volt watt (tests 26-31)

Smart-grid feature tests for stability check, unintended island prevention, ramp rates & soft start, and specified power factor were conducted separately.

Controller HIL was also used to test control stability under irradiance variations and MPPT action. The microinverter control system should track rapid transients in solar irradiance levels. Specifically, sharp negative transients in irradiance levels should not cause the converter to draw short-circuit current from the PV, which could result in substantial drop of PV voltage and possible reset of microinverter control. Additionally, positive transients should result in steady increases in power. A specific stability concern of the selected microinverter circuit design is that the APD and DAB control respond fast enough to prevent drawing excess power from the PV during negative irradiance transients. Due to the extensive use of feed-forward controls, these disturbances are readily mitigated.

Fig. 6 shows an example MPPT test where solar irradiance levels of the PV model are varied manually to emulate realistic variations of a PV source, and the microinverter responds

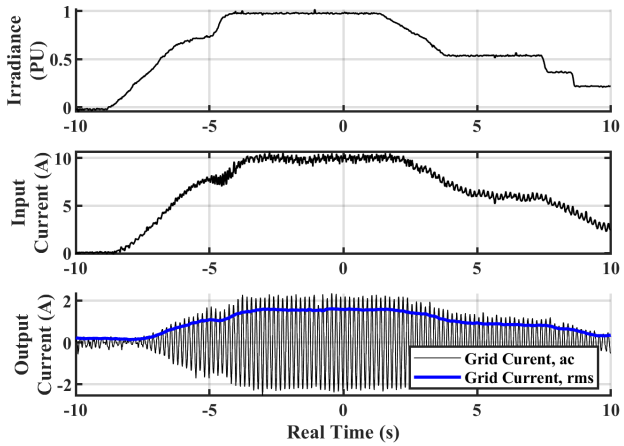

Fig. 6. Maximum power point tracking test using CHIL. Shown plots are normalized solar irradiance levels (upper), input current from the PV (middle), and output grid current (lower).

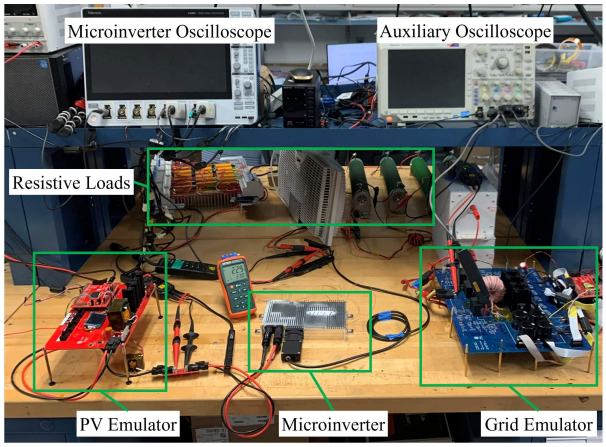

Fig. 7. Photo of complete hardware test configuration, including PV emulator, microinverter, and grid emulator.

accordingly. The irradiance is shown in per unit (pu) terms, where 1 pu is equal to the full power capability of the PV i.e., 400 W. Here the 10:1 time factor approach is used, so the 20 seconds of real-time data corresponds to 2 seconds of control and simulated time. Here it is shown that rapid transients in irradiance are tracked in a stable manner, even for changes in excess of 100% irradiance per second.

B. Hardware Testing

In the meantime of controller design and CHIL verification, the microinverter hardware was designed and constructed. Once both hardware and control were confidently functional, they were integrated for microinverter system testing. An incremental integration and test approach was used to ensure proper system integration. Fig. 7 shows the final hardware testing configuration. This test setup includes the proposed next-generation microinverter design, a custom-designed PV emulator, and a custom-designed grid emulator. This grid emulator shown is a unidirectional inverter, so a resistive load is connected in parallel to ensure power was only exported from the grid emulator.

Smart-grid compatibility was verified in hardware by confirming the individual required functionalities required, rather than repeating the exhaustive smart-grid feature testing that was performed in CHIL. This approach reduced hardware testing time and mitigated the risk of microinverter prototype destruction, which would significantly delay prototype development. The main functionalities required for smart-grid compatibility are reactive power injection / absorption, grid tracking, and operation at out-of-nominal grid conditions. If the converter can meet these conditions, then it is assumed that the hardware prototype would also meet the smart-grid tests performed in CHIL. Fig. 8 shows the range of required reactive power injection/absorption. To meet Volt/var smart-grid requirements of [6], 0.3 pu reactive power must be either absorbed or injected based on the magnitude of grid voltage. Additionally for specified power factor operation, the microinverter must also output a specified amount of reactive power. Fig. 9 shows several example ride-through tests. Fig. 9 (a) is a frequency ride-through test, where the grid frequency shifts from the nominal 60 Hz to 62 Hz. Accordingly, the converter maintains operation for approximately 0.16 seconds before tripping. Fig. 9 (b) shows a voltage ride-through test where grid voltage again reduces to 40% of the nominal voltage and returns to nominal in less than 1 second. Accordingly, the microinverter does not trip, and continues to operate after the grid recovers. Had the grid voltage not returned to nominal after 1 second, the microinverter would have been required to trip.

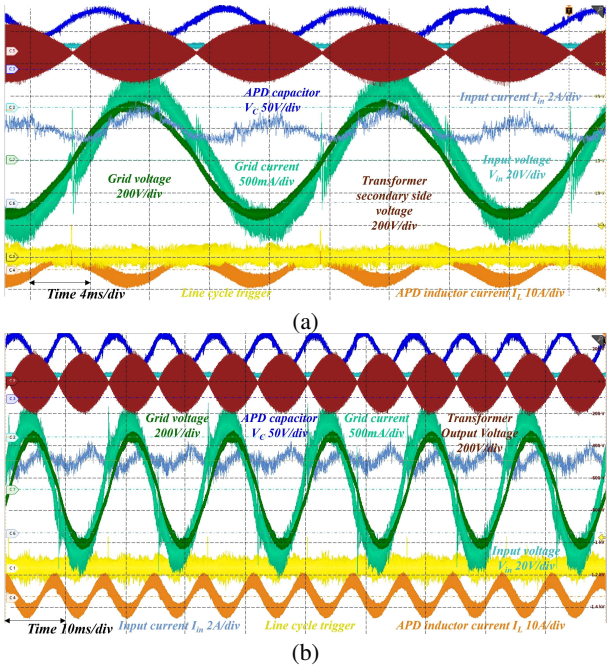

Fig. 8. Hardware testing results showing operation at the maximum required reactive power (0.3 pu or equivalently 120 var) in the case of a (a) lagging power factor and (b) leading power factor.

Maximum power point tracking performance was also con-

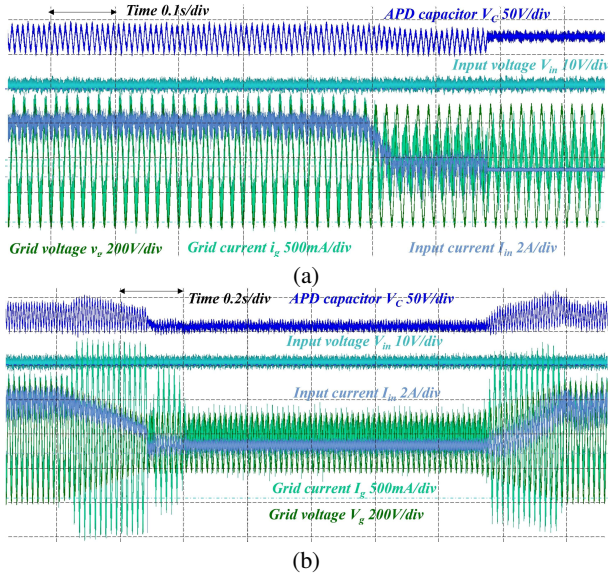

Fig. 9. Hardware transient response of (a) frequency ride through and trip (b) voltage ride through and recovery.

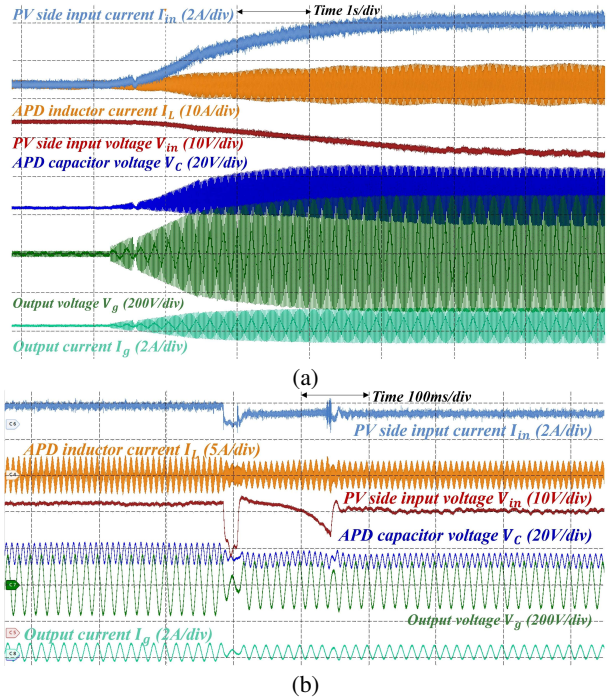

Fig. 10. Microinverter transient response with PV source and resistive load for (a) microinverter startup and (b) a negative step-change in the PV emulator's solar irradiance.

firmed in hardware. Fig. 10 (a) demonstrates MPPT tracking behavior of the microinverter hardware during startup. In this test, a PV emulator is used with steady irradiance levels. Initially the microinverter is idle, then it begins ramp power according to smart-grid requirements and MPPT commands. The P&O MPPT and voltage control action can be observed in the input voltage waveform. Fig. 10 (b) shows the microinverter's response to a step-drop in irradiance. Initially input voltage drops approximately 40% but recovers in less than 50 ms, verifying the desired MPPT operation.

IV. Conclusions

This paper presented the control system for a next-generation microinverter design and shows test results which verify adherence to smart-grid features and other next-generation microinverter performance targets. Successful CHIL testing, in conjunction with hardware demonstrations, verifies smart-grid compatibility and system stability during MPPT and irradiance disturbances. This successful system development and testing results demonstrates HIL's utility in complex power electronics control design and implementation. Similar approaches shall be considered for power converter design processes, specifically when implementing new control approaches, designing for high power, testing rare operating conditions, or if damage to hardware is of concern.

References

[1] REN21 Secretariat, "Renewables 2022 global status report," REN21, 2022.

[2] S. B. Kjaer, J. K. Pedersen, and F. Blaabjerg, "A review of single-phase grid-connected inverters for photovoltaic modules," IEEE Trans. Ind. Appl., vol. 41, no. 5, pp. 1292–1306, Sep. 2005, doi: 10.1109/TIA.2005.853371.

[3] K. Alluhaybi, I. Batarseh, and H. Hu, "Comprehensive review and comparison of single-phase grid-tied photovoltaic microinverters," IEEE J. Emerg. Sel. Top. Power Electron., vol. 8, no. 2, pp. 1310–1329, Jun. 2020, doi: 10.1109/JESTPE.2019.2900413.

[4] Q. Li and P. Wolfs, "A review of the single phase photovoltaic module integrated converter topologies with three different DC link configurations," IEEE Trans. Power Electron., vol. 23, no. 3, pp. 1320–1333, May 2008, doi: 10.1109/TPEL.2008.920883.

[5] B. Enayati, "Impact of IEEE 1547 standard on smart inverters and the applications in power systems," p. 87.

[6] California Public Utilities Commission, "Rule 21 interconnection." https://www.cpuc.ca.gov/Rule21/ (accessed Jul. 19, 2022).

[7] "IEEE SA - IEEE 1547-2018," IEEE Standards Association. https://standards.ieee.org/ieee/1547/5915/ (accessed Jul. 19, 2022).

[8] B. Lu, X. Wu, H. Figueroa, and A. Monti, "A low-cost real-time hardware-in-the-loop testing approach of power electronics controls," IEEE Trans. Ind. Electron., vol. 54, no. 2, pp. 919–931, Apr. 2007, doi: 10.1109/TIE.2007.892253.

[9] G. G. Parma and V. Dinavahi, "Real-time digital hardware simulation of power electronics and drives," IEEE Trans. Power Deliv., vol. 22, no. 2, pp. 1235–1246, Apr. 2007, doi: 10.1109/TPWRD.2007.893620.

[10] A. S. Vijay, S. Doolla, and M. C. Chandorkar, "Real-time testing approaches for microgrids," IEEE J. Emerg. Sel. Top. Power Electron., vol. 5, no. 3, pp. 1356–1376, Sep. 2017, doi: 10.1109/JESTPE.2017.2695486.

[11] M. Steurer, F. Bogdan, W. Ren, M. Sloderbeck, and S. Woodruff, "Controller and power hardware-in-loop methods for accelerating renewable energy integration," in 2007 IEEE Power Engineering Society General Meeting, Jun. 2007, pp. 1–4. doi: 10.1109/PES.2007.386022.

[12] J. Saha, G. N. Brahmendra Yadav, and S. Kumar Panda, "A review on bidirectional matrix-based AC-DC conversion for modular solid-state-transformers," in 2019 IEEE 4th International Future Energy Electronics Conference (IFEEC), Nov. 2019, pp. 1–8. doi: 10.1109/IFEEC47410.2019.9015013.

[13] Y. Shen, M. D'Antonio, S. Chakraborty, A. Hasnain, and A. Khaligh, "Comparison of CCM- and CRM-based boost parallel active power decoupler for PV microinverter," IEEE Trans. Power Electron., vol. 37, no. 8, pp. 9889–9906, Aug. 2022, doi: 10.1109/TPEL.2022.3158956.

[14] T. Esram and P. L. Chapman, "Comparison of photovoltaic array maximum power point tracking techniques," IEEE Trans. Energy Convers., vol. 22, no. 2, pp. 439–449, Jun. 2007, doi: 10.1109/TEC.2006.874230.

[15] "OP4510 V2 - Hardware products documentation - Wiki OPAL-RT." https://wiki.opal-rt.com/display/HDGD/OP4510+V2.